Nanoscale Advances

ROYAL SOCIETY OF CHEMISTRY

PAPER

View Article Online
View Journal | View Issue

Cite this: *Nanoscale Adv.*, 2022, **4**, 1758

Ultra-small-sized multi-element metal oxide nanofibers: an efficient electrocatalyst for hydrogen evolution†

Peng Liu,[a] Changchun Sun,[a] Guiju Liu,[b] Zhan Jiang*[a] and Haiguang Zhao *[ab]

Received 14th February 2022
Accepted 22nd February 2022

DOI: 10.1039/d2na00100d

rsc.li/nanoscale-advances

Compared to noble metals, transition metal oxides (TMOs) have positive development prospects in the field of electrocatalysis, and the synergy between the elements in multi-element TMO-based materials can improve their catalytic activity. However, it is still a challenge to synthesize multi-component TMO-based catalysts and deeply understand the effects of components on the catalytic performance of the catalysts. Here, we demonstrate multi-element ultra-small-sized nanofibers for efficient hydrogen production. The ternary NiFeCoO nanofiber-based electrode reached an overpotential of 82 mV at the current density of 10 mA cm^{-2} with a Tafel slope of 56 mV dec^{-1} in 1 M KOH, which are close to those of Pt plate (66 mV at 10 mA cm^{-2}; the Tafel slope is 32 mV dec^{-1}). In addition, the current density maintained 97% of its initial value after 10 h operation. We used the ternary NiFeCoO nanofiber-based electrode as an efficient counter electrode in photoelectrochemical hydrogen production to demonstrate the versatility of these nanofibers.

1. Introduction

The rapidly growing concerns of the energy crisis and global warming have inspired researchers to develop efficient technologies for obtaining renewable and clean energy to replace traditional fossil fuels. As a zero-carbon-emission green energy carrier, hydrogen energy has attracted much attention. The use of hydrogen energy does not result in any pollution, and its by-product of water can be recycled easily.[1] Solar-driven water electrolysis can produce hydrogen economically and environmentally; therefore, the combination between a solar cell and water electrolyzer is particularly rational. Alternatively, in photoelectrochemical (PEC) cells, electricity generated from a solar cell can be utilized to drive electrochemical transformations.[2–4]

The real potential of water splitting is much higher than the theoretical potential value (1.23 V).[5] A key factor to realize high-efficiency water splitting systems is the development of highly active, stable, and low-cost electrocatalysts for the hydrogen evolution reaction (HER).[6] Currently, platinum-based catalysts are still the most effective electrocatalysts for HER. However, Pt plate-based electrocatalysts suffer from the prohibitive cost and scarcity of Pt, which limits their commercial use for industry.[7]

Compared to noble metal-based catalysts, non-noble metal catalysts have been attracting much attention because of their excellent catalytic performance.[8–14] Among them, earth-abundant transition metal (M = Fe, Co and Ni)-based materials, including transition metal alloys,[9] oxides,[10] hydroxides,[11] phosphides,[12] sulfides[13] and nitrides,[14] have been extensively studied as water-splitting electrocatalysts.[9–17] Compared with other types of metal compounds, the compositions and structures of transition metal oxide (TMO) are more diverse, providing electronic and crystal structure flexibility with various ideal physical/chemical properties. In addition, TMOs are more competitive due to their low cost, earth abundant resources, flexible adjustability, environmental friendliness, good stability and ease of synthesis.[18–23] The HER catalytic performance of TMOs has been greatly improved through various strategies, such as doping,[24] oxygen-vacancy engineering,[25] morphology engineering,[26] and valence engineering.[6] Currently, different types of TMOs have been synthesized, including single metal oxides,[27] metal (hydroxy) hydroxides,[28] perovskite oxides,[29,30] spinel oxides,[31] and oxide-containing hybrids.[32] These materials may exhibit great potential as building blocks for HER. We summarized the catalytic performance of the TMO-based catalysts in Table S1.† Although researchers found that a Janus nickel–iron oxide nanoparticle catalyst exhibited an efficient HER with comparable performance to that of Pt/C,[33] it is still a challenge to synthesize multi-component ultra-small-sized TMO catalysts *via* a simple approach and deeply understand the effects of the components on the catalytic performance of the catalysts. Electrospinning technology can produce nano-structured one-dimensional nanofibers with multiple

[a]*College of Textiles & Clothing, Qingdao University, No. 308 Ningxia Road, Qingdao 266071, P. R. China. E-mail: kevinjiang_1987@126.com; hgzhao@qdu.edu.cn*

[b]*State Key Laboratory of Bio-Fibers and Eco-Textiles, Qingdao University, No. 308 Ningxia Road, Qingdao 266071, P. R. China*

† Electronic supplementary information (ESI) available. See DOI: 10.1039/d2na00100d

compositions with continuous processing.[34] After sintering, the nanofibers have a high specific surface area, aspect ratio, and porosity, as well as a large number of active sites.[35–39] There are still few reports of the preparation of binary and ternary TMO-based nanofibers as catalysts for use in the HER.

In this study, we demonstrated the fabrication of binary oxides (Fe_xCo_yO, Fe_xNi_yO, Co_xNi_yO) and ternary $Ni_xFe_yCo_zO$ nanofibers for effective generation of H_2 under alkaline conditions. These as-prepared nanofibers with an average diameter of 100 nm were prepared *via* electrospinning using renewable cellulose acetate (CA) and acetylacetone metal salts as spinning solutions and further sintered at 450 °C. Compared to single metal oxide-based catalysts, the binary and the ternary metal oxide-based catalysts exhibited better catalytic performance. The samples of NiFeCoO and FeCoO nanofibers coated on Ni foam (NiFeCoO-NF and FeCoO-NF) achieved a benchmark HER current density of 10 mA cm^{-2} with overpotentials of 42.4 mV and 66.4 mV in 1 M KOH solution, respectively. The synergistic effect of the different metal oxides explained the improved catalytic performance of the obtained catalysts. Furthermore, we expanded the application of the ternary metal oxide nanofiber-based electrodes as the counter electrode in photo-electrochemical (PEC) H_2 production using quantum dots/TiO_2 as the photoanode and Na_2S/Na_2SO_3 as the electrolyte to demonstrate the versatility of these nanofibers.

2. Results and discussion

2.1 Fabrication and structure of the as-prepared nanofibers

Electrospinning was used to produce hybrid nanofibers from a precursor solution containing CA and Co/Fe/Ni salts. Tin paper was used to collect the nanofibers. The obtained thin membrane was placed on the middle of the graphite plates to form a tandem structure, heated to 450 °C and maintained at this temperature for 30 min in air to remove the CA. The detailed preparation procedure is illuminated in Fig. S1.† With an identical preparation procedure, we could not obtain the CoO nanofibers; instead, nanobelts were observed, as shown in Fig. S2.† In order to fairly compare the catalytic properties of the as-prepared nanofibers with different compositions, we designed and prepared unary metal oxides (FeO and NiO), binary metal oxides (Fe_xCo_yO, Fe_xNi_zO and Co_yNi_zO) and ternary metal oxides ($Ni_xFe_yCo_zO$).

By optimizing the electrospinning parameters (*e.g.* voltage and moisture), the electrospun nanofibers had typical diameters in the range of 70–105 nm (Fig. S3, Table S2†), which could

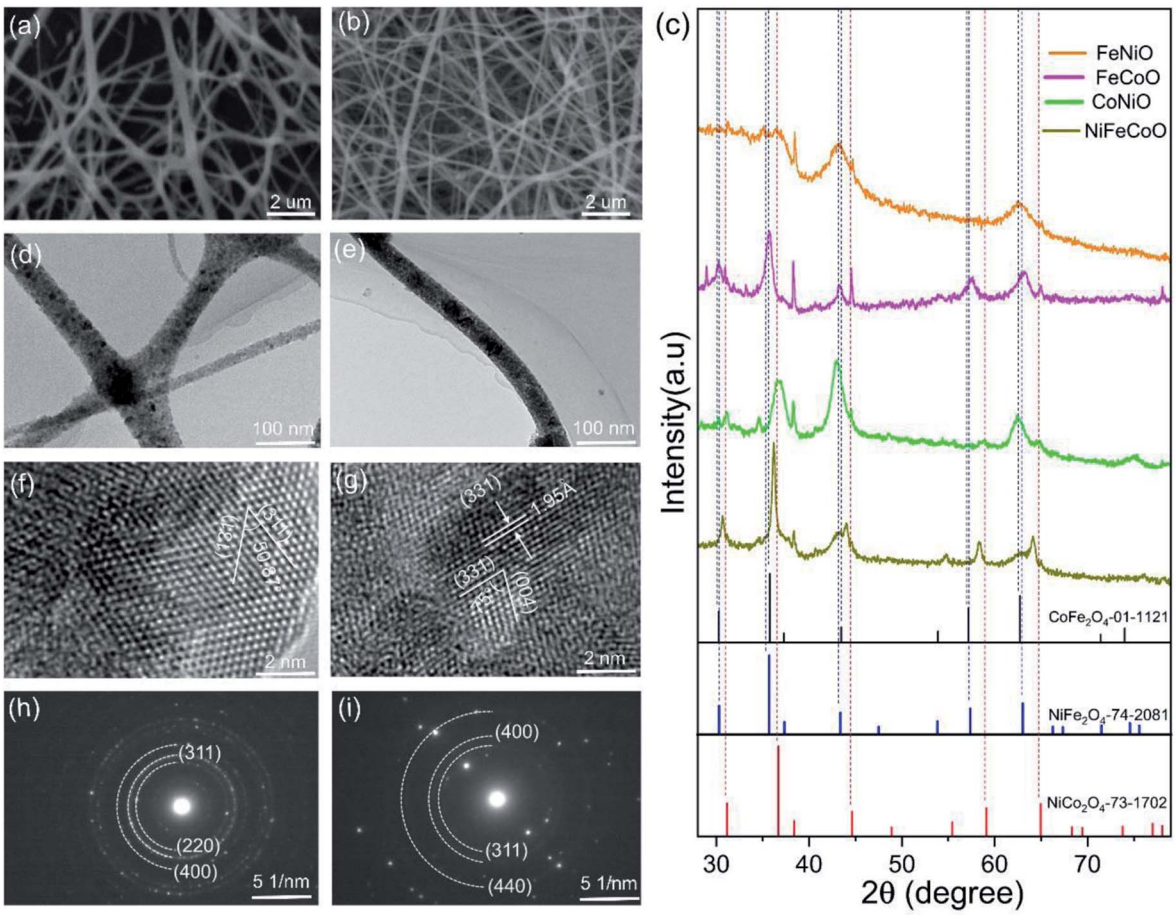

Fig. 1 SEM images of the (a) FeCoO and (b) NiFeCoO samples. (c) XRD patterns of the FeNiO, FeCoO, CoNiO and NiFeCoO samples. TEM images of the (d) FeCoO and (e) NiFeCoO samples. HRTEM images of the (f) FeCoO and (g) NiFeCoO samples. SAED patterns of the (h) FeCoO and (i) NiFeCoO samples.

result in their greater surface areas compared to nanofibers with large diameters. Fig. S4† shows a typical SEM image of the FeO and NiO samples with average diameters of 75 ± 20 nm and 95 ± 26 nm, respectively. As shown in Fig. 1a, the FeCoO nanofibers showed uneven fiber fineness and random distribution with a web-like morphology, with a typical diameter of 85 ± 27 nm. Fig. S5a† shows a typical SEM image of the FeNiO sample, with an overall diameter of 75 ± 20 nm. The CoNiO fibers have an average diameter of 85 ± 30 nm (Fig. S5b†). The SEM image of the NiFeCoO fibers showed a similar morphology to that of the FeNiO sample, with a mean diameter of 65 ± 17 nm (Fig. 1b). The presence of Fe, Co, and Ni elements was observed in the EDX patterns and XPS spectra for all the types of samples (Fig. S6–S17†).

To investigate the crystallite structure of the different obtained nanofibers, XRD patterns of these samples were obtained. Fig. S18† confirms that the FeO sample is hexagonal Fe_2O_3 (PDF 89-0597), and the NiO sample is cubic NiO (PDF 73-1523). Fig. 1c shows the typical XRD patterns of the binary and ternary metal oxide samples (FeCoO, FeNiO, CoNiO and NiFeCoO). The peaks at 30.3°, 35.7°, 43.2° and 63.2° of the FeCoO sample are assigned to the (220), (311), (400) and (440) planes of cubic $CoFe_2O_4$ (PDF 01-1121). For the FeNiO sample, the peaks at 30.4°, 35.1°, 43.3° and 62.8° are assigned to the (220), (311), (400) and (440) planes of cubic $NiFe_2O_4$ (PDF 74-2081). Similarly, the peaks of the CoNiO sample at 31.2°, 36.8° and 43° correspond to the (220), (311) and (400) planes of cubic $NiCo_2O_4$ (PDF 74-2081). For the XRD pattern of the NiFeCoO sample, the diffraction peaks are among those of $CoFe_2O_4$, $NiFe_2O_4$ and $NiCo_2O_4$. All the samples exhibited peaks at 38°, 45° and 65°. These peaks are assigned to the diffraction peaks of Al. During the electrospinning process, Al foil was used to collect the fibers. Al foil should be present in the samples for XRD measurements. Meanwhile, during further experiments, we sonicated the powders and centrifuged the samples dispersed in ethanol. We found that very small Al fragments were precipitated on the bottom of the tubes, confirming the existence of Al in the samples. We did not detect the signal of Al in the samples for the electrodes due to the efficient separation. Based on the XRD diffraction peaks, we calculated the average crystal sizes of the six samples according to the Scherrer equation. The FeO, NiO, FeCoO, FeNiO, CoNiO and NiFeCoO samples have average crystal sizes of 23.72, 10.26, 12.52, 10.93, 8.97 and 19.89 nm, respectively (Fig. S19†). Except for the FeO and NiFeCoO samples, all the samples have typical crystal sizes in the range of 9–13 nm. The formation of larger sizes in the NiFeCoO sample compared to the binary samples may be due to the lower concentration of each precursor, which could affect the process of nucleation and growth.

The TEM results reveal that the unary Fe_2O_3 and NiO nanofibers have very small diameters (less than 50 nm) with clear lattice fringes and diffraction patterns (Fig. S20†-21), which is consistent with the XRD results. The TEM images of FeCoO, FeNiO and CoNiO show a similar morphology to the NiO sample (Fig. 1d, S22 and S23†). The HRTEM image of the FeCoO sample reveals clear lattice fringes with distances of 2.53 Å and 2.52 Å and an angle of 50.87°, which match well with the (311) and (131) planes of $CoFe_2O_4$ (PDF 01-1121) (Fig. 1f). The SAED pattern further confirms the presence of FeCoO, FeNiO and CoNiO cubic crystals (Fig. 1h, S22 and S23†).

Fig. 1e shows a typical TEM image of the NiFeCoO nanofibers, which shows that the diameter of the NiFeCoO nanofibers is about 50 nm. Fig. 1g shows the HRTEM image of the NiFeCoO nanofibers. The lattice spacings of the two planes with an angle of 75° were measured to be 1.95 Å and 2.28 Å. According to the XRD results, we found that the structures of $CoFe_2O_4$, $NiFe_2O_4$ and $NiCo_2O_4$ are very similar ($CoFe_2O_4$ PDF 01-1121: $a = b = c = 8.39$, $\alpha = \beta = \gamma = 90°$; $NiFe_2O_4$ PDF 74-2081: $a = b = c = 8.3379$, $\alpha = \beta = \gamma = 90°$; $NiCo_2O_4$ PDF 73-1702: $a = b = c = 8.114$, $\alpha = \beta = \gamma = 90°$). Therefore, the two planes labeled in Fig. 1g can be indexed to the (331) and (004) planes of $CoFe_2O_4$, $NiFe_2O_4$ or $NiCo_2O_4$. The SAED pattern also reflects the same information (Fig. 1i). The slightly diffused rings were indexed to the (311), (400) and (440) planes of $CoFe_2O_4$, $NiFe_2O_4$ or $NiCo_2O_4$. Because the EDX pattern and XPS spectrum of the NiFeCoO sample confirmed the existence of Fe, Co, Ni and O elements (Fig. S16 and S17†), we inferred that the products of the NiFeCoO sample were mixture phases of $CoFe_2O_4$, $NiFe_2O_4$ and $NiCo_2O_4$. This is also consistent with the XRD analysis.

High-resolution Fe, Co and Ni XPS spectra were used to further determine the surface status of the samples. The high-resolution Fe 2p, Co 2p and Ni 2p spectra of all the samples show spin–orbit splitting into $2p_{1/2}$ and $2p_{3/2}$ components (Fig. 2a–k). The satellite peaks were found for all the samples. For the nanofibers containing Fe element, the high resolution $2p_{1/2}$ peaks of the FeO sample at 724.08 eV and 724.48 eV, 724.33 eV and 724.21 eV correspond to FeCoO, FeNiO, and NiFeCoO, respectively. The slight increase in binding energy indicates the variation of the valence state of Fe in the different components. For Co element, the $2p_{1/2}$ peak of the FeCoO sample was located at 796.78 eV. In contrast, the $2p_{1/2}$ peak of the CoNiO sample was located at 796.37 eV, indicating that the valence states of Co element in the two samples are different. Furthermore, the Co 2p spectrum of the NiFeCoO sample can be fitted into eight separate peaks: the peak at 796.14 eV is ascribed to Co^{3+} $2p_{1/2}$ and the peak at 797.24 eV corresponds to Co^{2+} $2p_{1/2}$, which implies that there are two valence states of Co element in the NiFeCoO sample, consistent with the XRD findings ($CoFe_2O_4$ and $NiCo_2O_4$). The $2p_{1/2}$ peaks of the NiO, FeNiO, CoNiO and NiFeCoO samples are located at 872.73 eV, 872.93 eV, 873.05 eV and 871.79 eV, which correspond to NiO, FeNiO, CoNiO and NiFeCoO, respectively. These results indicated that the binding energy between Fe/Co/Ni and O is slightly different among the TMOs with different compositions, which might affect the HER activity. Based on the XPS results, we also calculated the element ratios, as shown in Table S3.† The element ratio of Fe/Co is 1 : 1.39 in the FeCoO sample, and that of Fe/Ni in the FeNiO sample is 1.66 : 1. The element ratio of Co/Ni in the CoNiO sample is 1 : 1.06 and that of Fe/Co/Ni in the NiFeCoO sample is 1.16 : 1.31 : 1.

2.2 HER performance

To investigate the HER catalytic performance, the LSV curves were measured over the nanofibers and a Pt plate catalyst. Six

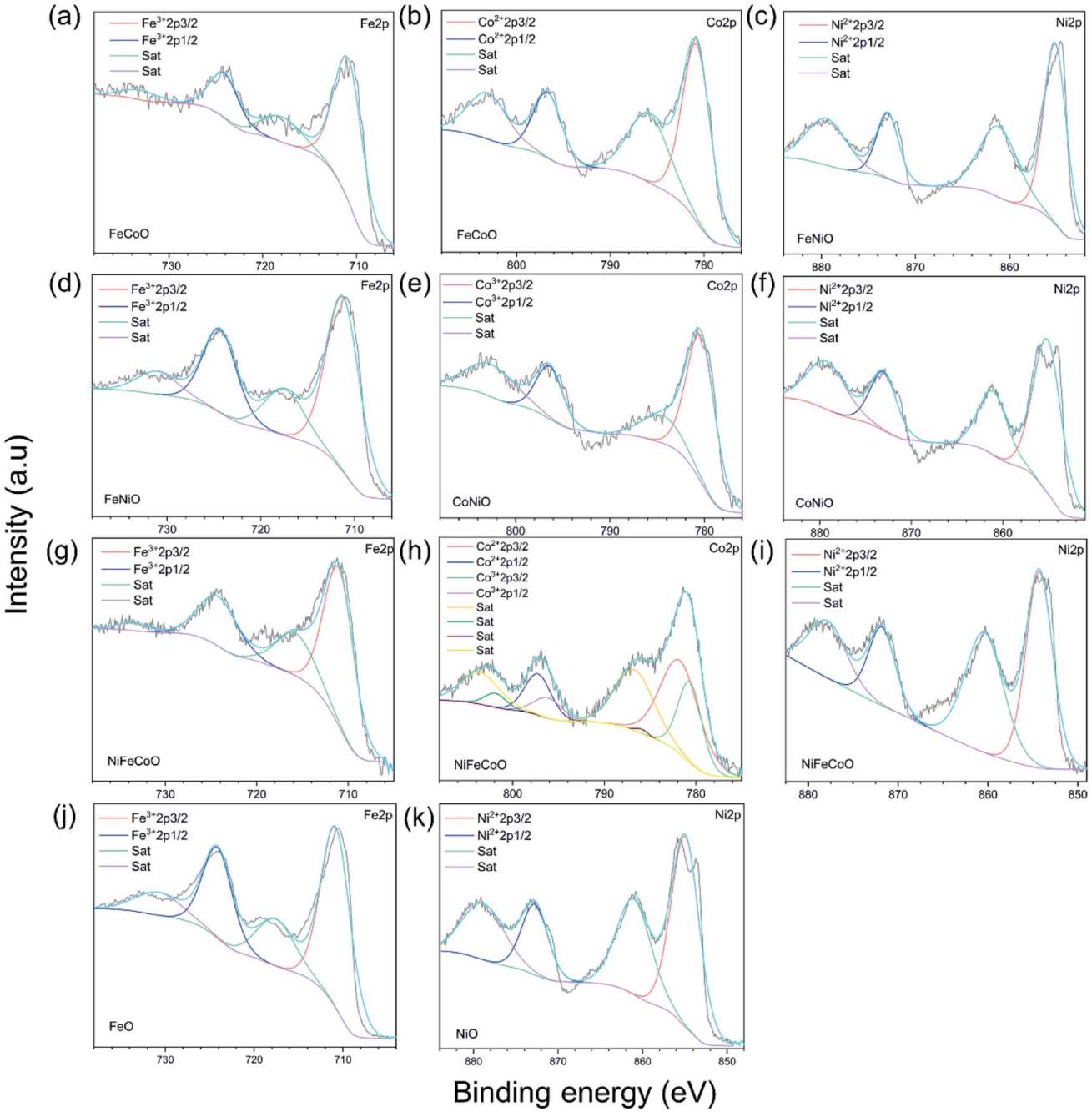

Fig. 2 (a and b) Fe 2p and Co 2p high-resolution XPS spectra of the FeCoO sample. (c and d) Ni 2p and Fe 2p high-resolution XPS spectra of the FeNiO sample. (e and f) Co 2p and Ni 2p high-resolution XPS spectra of the CoNiO sample. (g–i) Fe 2p, Co 2p and Ni 2p high-resolution XPS spectra of the NiFeCoO sample. (j) Fe 2p high-resolution XPS spectra of the FeO sample. (k) Ni 2p high-resolution XPS spectra of the NiO sample.

different samples were drop-dried on glassy carbon electrode for testing in 1 M KOH (Fig. 3a). The NiFeCoO electrode and FeCoO electrode exhibited significantly improved activity, with overpotentials of 192 mV and 124 mV at the current density of 10 mA cm^{-2}; these are not as good as that of Pt plate (66 mV) but much higher than those of the other four samples. The overpotentials of 438 mV, 686 mV, 397 mV and 465 mV at the current density of 10 mA cm^{-2} correspond to FeO, NiO, FeNiO and CoNiO, respectively.

In addition, the NiFeCoO electrode and FeCoO electrode exhibited excellent catalytic performance at high current density. At a current density of 50 mA cm^{-2}, their overpotentials were 312 mV (NiFeCoO) and 243 mV (FeCoO), which were much lower than the overpotential of Pt plate (424 mV) and of the other four samples [566 mV (FeO), 883 mV (NiO), 582 mV (FeNiO) and 578 mV (CoNiO)].

As shown in Fig. 3b, the FeCoO catalysts have the smallest Tafel slope (82 mV dec^{-1}), suggesting more favorable HER

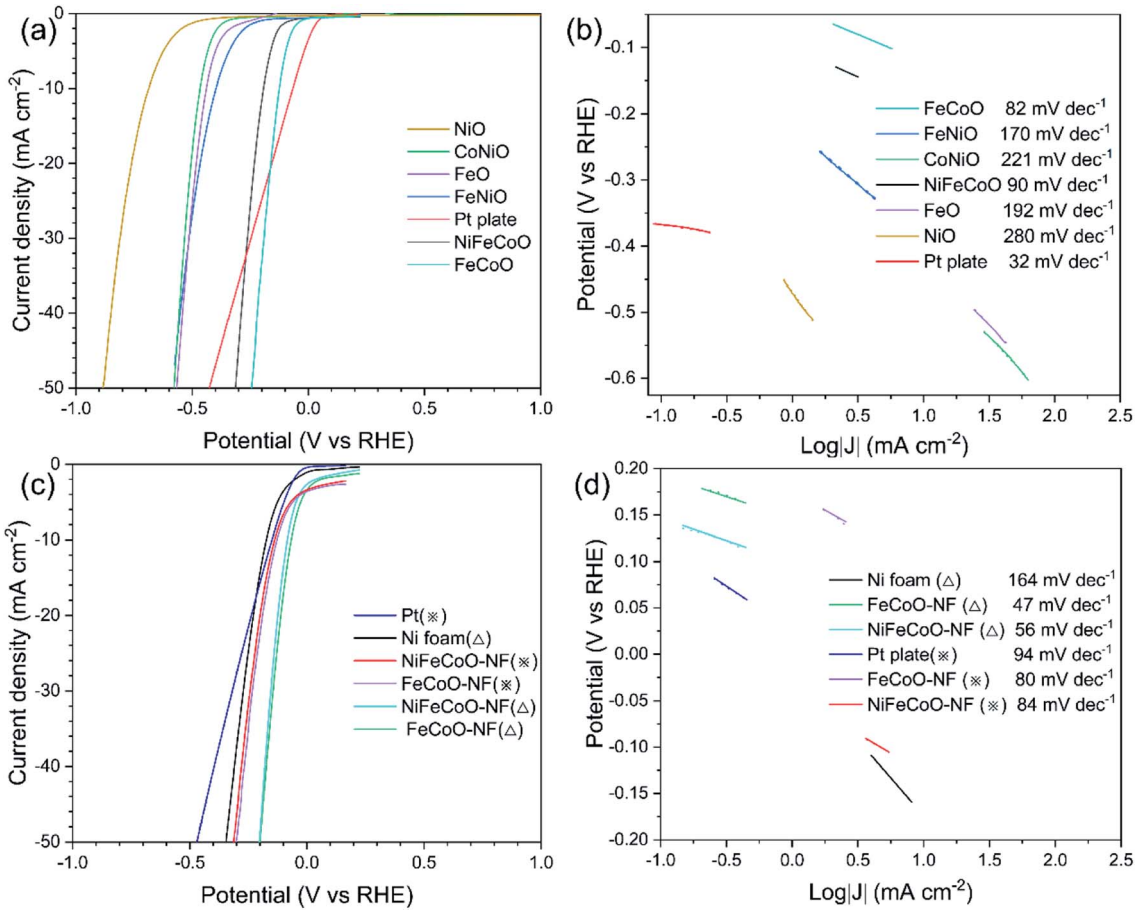

Fig. 3 (a) Polarization curves for NiO, CoNiO, FeO, FeNiO, Pt plate, NiFeCoO and FeCoO samples in 1.0 M KOH. (b) Tafel plots of the Pt plate, FeCoO, FeNiO, CoNiO, NiFeCoO, FeO and NiO samples in 1.0 M KOH. (c) Polarization curves for the Pt plate, Ni foam, FeCoO-NF and NiFeCoO-NF samples. (d) Tafel plots of the Pt plate, Ni foam, FeCoO-NF and NiFeCoO-NF samples. (△) Experiments were performed in 1.0 M KOH; (※) experiments were performed in 0.25 M Na_2S/0.35 M Na_2SO_3.

reaction kinetics than that of the other samples. The NiFeCoO catalysts have a Tafel slope of 90 mV dec^{-1}. Although the Tafel slopes of FeCoO and NiFeCoO are not comparable to that of the Pt plate electrode (32 mV dec^{-1}), these results implied that samples containing Fe and Co elements have higher catalytic activity than those containing Ni, consistent with the reported results in the literature.[40–42] The HER catalytic performance of the unary samples was lower compared to that of the binary and ternary samples, which can be attributed to the lack of synergy between the elements.

To further improve the catalytic performance of the nanofibers, we deposited the nanofibers onto Ni foam (NiFeCoO-NF and FeCoO-NF). As shown in Fig. 3c, the overpotentials of NiFeCoO-NF and FeCoO-NF reached 82 mV and 66 mV, respectively, at the current density of 10 mA cm^{-2}, which are comparable to that of Pt plate (66 mV). For comparison, we also measured the overpotential of the Ni foam, which showed 172 mV at the current density of 10 mA cm^{-2} in 1 M KOH. At a current density of 50 mA cm^{-2}, their overpotentials reached 210 mV (NiFeCoO-NF), 199 mV (FeCoO-NF) and 344 mV (Ni foam), which are consistent with the trend at a current density of 10 mA cm^{-2}. In addition, in 0.25 M Na_2S/0.35 M Na_2SO_3 instead of 1 M KOH, NiFeCoO-NF also exhibited much smaller overpotentials (137 mV at 10 mA cm^{-2}; 312 mV at 50 mA cm^{-2}) than Pt plate (148 mV at 10 mA cm^{-2}; 469 mV at 50 mA cm^{-2}). Its Tafel slope is 56 mV dec^{-1} in 1 M KOH and 84 mV dec^{-1} in 0.25 M Na_2S/0.35 M Na_2SO_3. FeCoO-NF exhibited the smallest overpotentials (127 mV at 10 mA cm^{-2}; 301 mV at 50 mA cm^{-2}) in 0.25 M Na_2S/0.35 M Na_2SO_3. Although the Tafel slope of FeCoO-NF is not comparable to that of the commercial Pt/C electrode (31 mV dec^{-1}), its Tafel slope (47 mV dec^{-1} in 1 M KOH and 80 mV dec^{-1} in 0.25 M Na_2S/0.35 M Na_2SO_3) is still lower than that of other samples, as shown in Fig. 3d and S24.†

To investigate the component effects of different components of binary and ternary metal oxides, the FeCoO samples were fabricated with identical Fe contents, but different cobalt contents (Fig. S25†). The overpotential value of the FeCoO sample (Fe : Co = 2 : 1) was higher than that of the FeCoO sample (Fe : Co = 2 : 2) at the current density of 10 mA cm^{-2} in 1 M KOH (279 for the former and 124 mV for the latter). At a current density of 50 mA cm^{-2}, their overpotentials reached 374 mV [FeCoO (Fe : Co = 2 : 1)] and 243 mV [FeCoO (Fe : Co = 1 : 1)], which are consistent with the trend at a current density

of 10 mA cm^{-2}. This result confirms that Co has better catalytic activity compared to Fe in FeCoO.

To investigate the relationship between the average diameter and the catalytic performance, new NiFeCoO samples were fabricated with different diameters (Fig. S26†). The overpotential of NiFeCoO (65 ± 17 nm) reached 192 mV at the current density of 10 mA cm^{-2} in 1 M KOH, which is lower than that of NiFeCoO (110 ± 30 nm) (397 mV). At a current density of 50 mA cm^{-2}, their overpotentials reached 312 mV NiFeCoO (65 ± 17 nm) and 511 mV NiFeCoO (110 ± 30 nm), which are consistent with the trend at a current density of 10 mA cm^{-2}. With the decrease of the diameter, the overpotential of the electrode decreases. The specific surface area was calculated compared to that of the fiber with a diameter of 50 nm as a function of the fiber diameter, as shown in Fig. S27.† The result shows that the smaller the diameter of the fiber, the larger the specific surface area. It is implied that a smaller diameter fiber may increase the contact area and the density of the active sites, thereby increasing the catalytic activity.[43]

In order to understand the catalytic performance of the nanofibers, we studied the effect of the chemical composition by performing EIS measurements. The semicircle in the Nyquist plot, attributed to the charge transfer resistance R_{ct}, is related to the kinetics of the electron transfer, and a lower diameter semicircle corresponds to a faster reaction rate.[44] The EIS curves were modeled using a simplified Randles equivalent circuit, which consists of a resistor in series (R_s) with a parallel arrangement of a resistor (R_{ct}) and a constant phase element (Fig. 4d).

As shown in Fig. 4a, the FeCoO and NiFeCoO coated glassy carbon electrodes exhibited smaller R_{ct} values of 25.86 Ω and 37.78 Ω, respectively, compared to the electrodes based on FeNiO (344.63 Ω) and CoNiO (442.28 Ω) in 1 M KOH (see the summary in Table S4†). For the nanofibers deposited on the Ni foam, FeCoO-NF and NiFeCoO-NF held R_{ct} values of 7.91 Ω and 12.1 Ω, compared with Ni foam (17.4 Ω) and Pt plate (1.38 Ω), in 1 M KOH (Fig. 4b and Table S5†); this suggests that the Ni foam can enhance the rate of electron transfer. In addition, the FeCoO-NF and NiFeCoO-NF-based electrodes exhibited R_{ct} values of 9.18 Ω and 13.02 Ω in 0.25 M Na_2S/0.35 M Na_2SO_3 (Fig. 4c and Table S6†).

These EIS results explain the trend of the overpotentials and Tafel plots for the nanofiber-based electrodes and prove that the FeCoO and NiFeCoO nanofiber-based electrodes have superior electron transfer properties, which is a very important factor for HER.

The stability of all the samples on the glassy carbon electrode was not good. The FeCoO and NiFeCoO samples only retained 71.7% and 91% of their original values, respectively, in 1 M KOH after 10 h of operation (Fig. S28†). This could be due to the

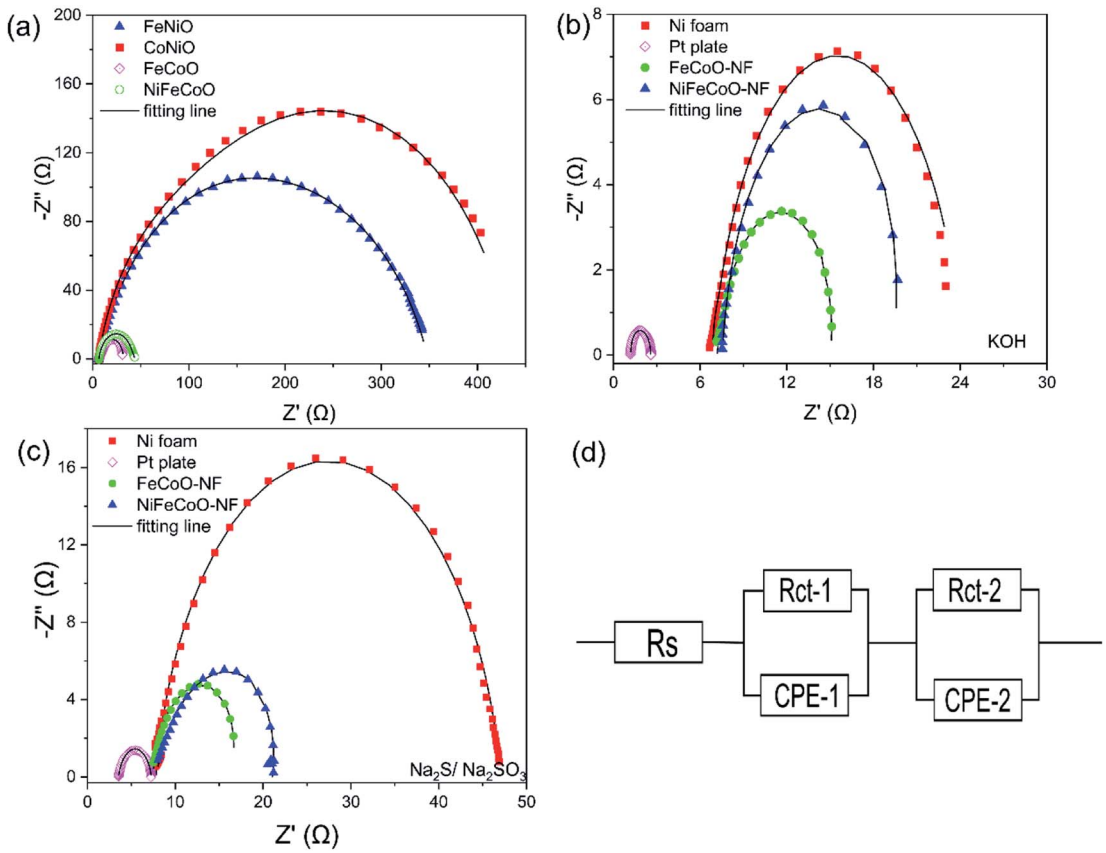

Fig. 4 (a) Nyquist plots of the FeNiO, CoNiO, FeCoO and NiFeCoO samples in 1 M KOH. (b) Nyquist plots of Ni foam, Pt plate, FeCoO-NF and NiFeCoO-NF in 1 M KOH. (c) Nyquist plots of Ni foam, Pt plate, FeCoO-NF and NiFeCoO-NF in 0.25 M Na_2S/0.35 M Na_2SO_3. (d) Equivalent circuit.

fact that the thin nanofiber/Nafion membrane does not have good attachment on the glassy carbon electrode. After a long-term stability test, some catalysts fell off the surface of the glassy carbon electrode, which would affect their stability.

To improve the catalytic stability, we replaced the glassy carbon electrode with porous Ni foam. Chronoamperometry measurements showed the catalytic stability of the Ni foam, as shown in Fig. 5b. The current density retained 61% of its original value in 1 M KOH. Meanwhile, the retained current density of the Ni foam increased to 58% of its original value in 0.25 M Na_2S/0.35 M Na_2SO_3, which can be attributed to the formation of highly catalytic Ni_xS. Impressively, the NiFeCoO coated on the Ni foam exhibited excellent long-term stability; it maintained 97% of its initial value in 1 M KOH and 97% in 0.25 M Na_2S/0.35 M Na_2SO_3 after 10 h of continuous testing (Fig. 5a), which is much better than Pt plate electrode (62.5% in 1 M KOH and 24.8% in 0.25 M Na_2S/0.35 M Na_2SO_3) (Fig. 5c). The improved stability in Ni foam suggests improved mechanical stability due to the intrinsic nature of the Ni foam. As shown in Fig. 5d, the current density of the FeCoO-NF based electrode retained 94% of its original value in 1 M KOH and 62% in 0.25 M Na_2S/0.35 M Na_2SO_3 after 10 h of continuous testing. The excellent stability of the nanofiber-based electrodes compared to Pt plate suggests that they are suitable for long-stable operation for H_2 production.

Additionally, the FeCoO-NF and NiFeCoO-NF electrodes exhibited enhanced stability for the HER, and their current density underwent almost no decay after 10 h of electrochemical testing (Fig. 5). As shown in Fig. S29,† after a 10 h test, we recorded the polarization curves of the electrodes. The overpotential of FeCoO-NF changed slightly (85 mV at a current density of 10 mA cm^{-2} and 264 mV at a current density of 50 mA cm^{-2}). The overpotential of NiFeCoO-NF was 99 mV at a current density of 10 mA cm^{-2}, and the overpotential changed more slightly at a current density of 50 mA cm^{-2} (220 mV). This result further showed that the FeCoO-NF and NiFeCoO-NF samples have good catalytic stability. In order to verify the good stability in the NiFeCoO-NF and FeCoO-NF samples, we explored the structure and composition changes of the sample after 10 hours of electrochemical testing, using HRTEM and XPS (Fig. S30 and S31†). We found that there was no significant structure or composition variation after 10 h testing, indicating that NiFeCoO-NF and FeCoO-NF are very stable during the HER.

The electrochemical active surface area (ECSA) plays a key role in high intrinsic HER activity.[45] To estimate the ECSAs of the catalysts under the working conditions, the electrochemical double-layer capacitance (C_{dl}) was measured by CV in a non-redox potential region (Fig. S32a and b†).[46] The linear slope is equivalent to twice the C_{dl}.[47] As shown in Fig. S32c,† the C_{dl} of FeCoO-NF was calculated to be 32.2 mF cm^{-2}, which is higher

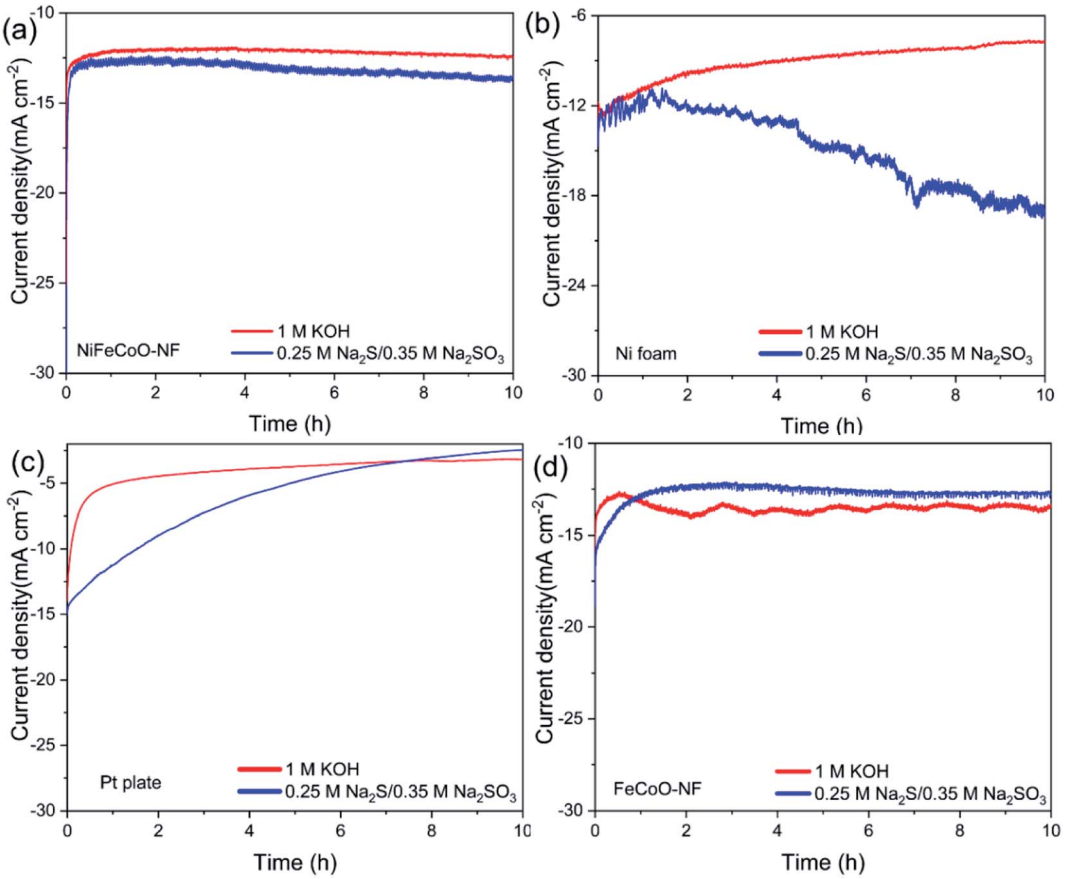

Fig. 5 (a–d) Chronopotentiometric curves of NiFeCoO-NF, Ni foam, Pt plate and FeCoO-NF obtained at a constant applied potential in 1 M KOH and 0.25 M Na_2S/0.35 M Na_2SO_3, respectively.

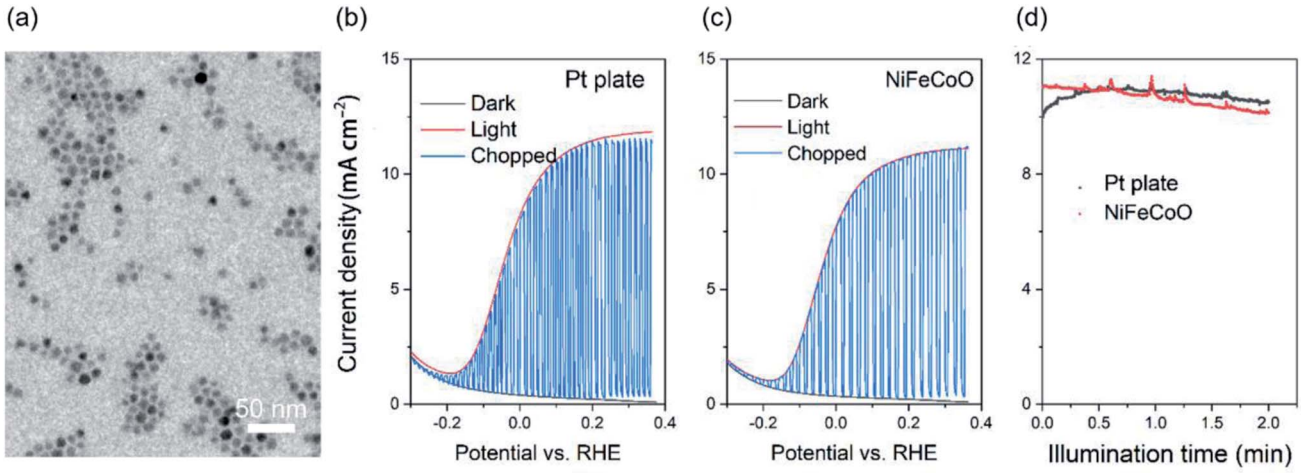

Fig. 6 (a) Transmission electron microscopy image of the CdSe/CdS QDs. (b and c) *J–V* (*versus* RHE) of CdSe/CdS@TiO_2-sensitized photoanodes in the dark as well as under continuous and chopped illumination (100 mW cm^{-2}) using Pt plate (b) and NiFeCoO nanofibers (c) as the counter electrode. (d) *J versus* illumination time at 0.3 V *versus* RHE under illumination (100 mW cm^{-2}).

than that of NiFeCoO-NF (30.3 mF cm^{-2}). The turnover frequency (TOF) values of FeCoO-NF and NiFeCoO-NF were calculated to be 0.131 s^{-1} and 0.107 s^{-1}, respectively, at an overpotential of 100 mV at pH 14 (Fig. S32d†), which confirms the high intrinsic catalytic HER activity of the FeCoO-NF and NiFeCoO-NF samples. Fe^{3+}, Co^{3+} and Co^{2+} can all promote the adsorption of water on the surface of a catalyst, which could facilitate the transfer of electrons to water molecules, thereby accelerating the Volmer reaction ($H_2O + e^- \rightarrow H^* + OH^-$). In addition, Ni^{2+} can act as an H* acceptor to further promote the Volmer reaction.[2,46] The synergy between the three elements of iron, cobalt and nickel promotes the progress of the catalytic reaction. Based on our results, the iron, cobalt and nickel oxides all serve as active centers, even though the catalytic activity of the iron and cobalt oxides is better than that of the nickel oxide. Generally, compared to a single metal oxide (*e.g.* NiO), the incorporation of Fe or Co can promote the adsorption of water on the surface of a catalyst; this can facilitate the transfer of electrons to water molecules, thereby accelerating the Volmer reaction.[2,46–48] As shown in Fig. 4a and Table S4,† the R_{ct} values of FeCoO (25.86 Ω) and NiFeCoO (37.78 Ω) are much lower than that of FeNiO (344.63 Ω) or FeNiO (442.28 Ω), confirming that the samples containing Fe and Co have better catalytic performance compared to the samples containing Ni.[2,46–48] In addition, the addition of Ni to the oxides can improve the stability of FeCoO. In summary, FeCoO-NF has higher HER catalytic activity than NiFeCoO-NF, but its long-term stability is not as good as that of NiFeCoO-NF in 1 M KOH and 0.25 M Na_2S/0.35 M Na_2SO_3. This can be attributed to the fact that the increase of cobalt content improves the catalytic activity, but the overactive catalytic activity leads to a decrease in stability. Combining the two indicators of catalytic activity and stability, NiFeCoO-NF is more suitable for use as a HER catalyst.

2.3 PEC performance

As a proof of concept, we used the as-fabricated ternary NiFeCoO nanofibers–Ni foam as a counter electrode for PEC hydrogen production. Platinum was used as the benchmark. A typical three three-electrode configuration was used for PEC hydrogen generation. A TiO_2 mesoporous film sensitized with CdSe/CdS quantum dots (QDs) was used as the photoanode, and saturated Ag/AgCl was used as the reference electrode. The electrolyte contained 0.25 M Na_2S and 0.35 M Na_2SO_3 (pH ~ 13). The typical morphology of CdSe/CdS is shown in Fig. 6a. Fig. 6b and c shows that the photocurrent density (*J*) is related to the amount of H_2 evolved at the counter-electrode. *J* reaches its saturation at ~11 mA cm^{-2} with a potential *vs.* RHE of 0.25 V, which is a slight decrease in *J* compared to that of Pt plate (11.5 mA cm^{-2}), indicating that the nanofiber-based counter electrode is suitable to replace the Pt plate. Similar behavior was obtained during long-term stability testing, as displayed in Fig. 6d, where *J* maintained 90% of its initial value after 2 h illumination. Considering that the nanofiber-based Ni foam has much better stability in the 0.25 M Na_2S and 0.35 M Na_2SO_3 electrolyte, the replacement of Pt plate with nanofibers may contribute to the potential commercial application of the QDs-based PEC hydrogen generation.

3. Conclusion and perspectives

In summary, we demonstrated multi-component TMO ultra-small-sized nanofibers for efficient HER. The nanofibers were prepared using environmentally friendly cellulose as the spinning solution *via* a simple electrospinning and further annealing approach. The as-prepared nanofibers have an ultra-small diameter of less than 105 nm with an average crystallite size of less than 25 nm. The binary and ternary TMO contained pure or mixture phases of $CoFe_2O_4$, $NiFe_2O_4$ and $NiCo_2O_4$. Benefiting from the synergy effect of multiple crystals, the NiFeCoO-NF based electrode achieved a current density of 10 mA cm^{-2} at a low overpotential of 82 mV with a Tafel slope ≈ 56 mV dec^{-1} in 1 M KOH, which are close to those of Pt plate. More importantly, the current density maintained 97.13% of its initial value after 10 h operation. In the PEC cell, the device has a *J* value of

~11 mA cm^{-2} and good stability in 0.25 M Na_2S and 0.35 M Na_2SO_3 upon 100 mW cm^{-2} illumination, which are comparable to those of a counter electrode using Pt plate. These results indicated that the current fabricated multi-element ultra-small-sized nanofibers are suitable as efficient catalysts for the HER. Considering the excellent catalytic properties of the binary and ternary nanofibers, they may be useful for Li-ion batteries, supercapacitors and CO_2 reduction.

4. Experimental section

4.1. Materials

CA (acetyl content 39.8 wt%, hydroxyl content 3.5 wt%), iron(III) acetylacetonate ($C_{15}H_{21}FeO_6$), cobalt(III) acetylacetonate ($C_{15}H_{21}CoO_6$), and nickel(II) acetylacetonate ($NiC_{10}H_{14}O_4$) were purchased from Aladdin Inc. Acetone and *N*,*N*-dimethylacetamide were purchased from Sinopharm Chemical Reagent Co. Ltd. All chemicals were used as purchased.

4.2 Preparation of nanofibers

Before the spinning process, a stock solution was prepared by mixing the metal salts with CA. For the binary and ternary metal oxide stock solutions, the mass ratio was 1 for all samples. Typically, CA (1.6 g) was dissolved in a mixed solution of acetone (5.32 g) and *N*,*N*-dimethylacetamide (2.68 g) with magnetic stirring for 4 h. Subsequently, $C_{15}H_{21}FeO_6$ (0.13 g), $C_{15}H_{21}CoO_6$ (0.13 g), and $NiC_{10}H_{14}O_4$ (0.13 g) were added to the CA solution, and the solution was maintained under stirring for 12 h. The as-prepared stock solution was further sonicated for 20 minutes before electrospinning. The stock solution was electrospun using an HZE (HZ-01) electrospinning unit with a 21 G needle at a flow rate of 0.2 mL h^{-1} and an applied voltage of 25 kV over a collection distance of 20 cm. The as-prepared nanofiber film was collected and calcined in a muffle furnace at 450 °C for 0.5 h with a heating rate of 1 °C min^{-1} under air atmosphere.

4.3 Preparation of nanofiber-based electrodes

One milligram of as-prepared nanofibers was mixed with 100 μL of a mixture of water, ethanol, and Nafion with a volume ratio of 1 : 8 : 1. Then, 20 μL of as-fabricated ink was dropped onto the glassy carbon electrode. For Ni foam, the thickness was 0.5 mm, and the front and back sides were sealed with epoxy glue, leaving only 0.25 cm^2 of exposed Ni foam on the front. Then, 60 μL of as-fabricated ink was dropped onto the Ni foam and dried naturally with a typical size of 0.25 cm^2.

4.4 Fabrication of PEC anode

A drop-casting approach was used to prepare TiO_2 mesoporous film.[49–51] The as-prepared CdSe/CdS QDs were synthesized and were dispersed in 50 mL toluene before electrophoretic deposition (200 V for 1 h).[52] Finally, two cycles of ZnS were coated on the photoanode using successive ionic layer adsorption and reaction.[52]

4.5 Structural characterizations

The morphology of the samples was characterized by field emission SEM using a JEOL JSM7001F FE-SEM equipped with an EDS. Transmission electron microscopy and SAED were performed using a JEOL JEM-2010 Plus TEM. XRD patterns were acquired using a Philips X' Pert diffractometer equipped with a Cu Kα radiation source ($\lambda = 0.15406$ nm). XPS was performed in a VG Escalab 220i-XL equipped with a hemispherical analyzer recorded for a twin anode X-ray source. The fine structure of the photoelectron lines was analyzed using Casa XPS software (2.3.19 version).

4.6 Electrochemical characterizations

The measurements were recorded using a CHI 760E electrochemical workstation. Electrochemical measurements were conducted at room temperature using 1 M KOH (50 mL, pH ≈ 14) and 0.25 M Na_2S/0.35 M Na_2SO_3 (50 mL, pH ≈ 13) as the electrolyte, respectively. A standard three-electrode setup was used with nanofibers, Pt plate, and Ag/AgCl (1 M KCl) acting as the working, counter, and reference electrodes, respectively.

EIS of the as-prepared nanofiber films was performed in potentiostatic mode at open circuit potential, applying a sinusoidal voltage with an amplitude of 10 mV and scanning frequency from 100 kHz to 100 mHz. The EIS was modeled using a simplified Randles equivalent circuit, which consists of a resistor in series (R_s) with a parallel arrangement of a resistor (R_{ct}) and a constant phase element, in Zview software. The LSV was performed with a scan rate of 5 mV s^{-1} in the voltage region of −800 to −1600 mV. Chronoamperometric curves (*I*–*t*) were measured with a constant current density to prove the stability of the as-prepared electrocatalysts.

Conflicts of interest

The authors declare no competing interests.

Acknowledgements

H. G. Zhao acknowledges the funding support from Shandong Natural Science Funds for Distinguished Young Scholar (ZR2020JQ20), State Key Laboratory of Bio-Fibers and Eco-Textiles (Qingdao University), No. ZKT03, ZFZ201807, and GZRC202004.

References

1 Z. Zhang, X. Wu, Z. Kou, N. Song, G. Nie, C. Wang, F. Verpoort and S. Mu, Rational design of electrospun nanofiber-typed electrocatalysts for water splitting: A review, *Chem. Eng. J.*, 2022, **428**, 131133, DOI: 10.1016/j.cej.2021.131133.

2 H. A. Bandal, A. R. Jadhav, A. H. Tamboli and H. Kim, Bimetallic iron cobalt oxide self-supported on Ni-Foam: An efficient bifunctional electrocatalyst for oxygen and hydrogen evolution reaction, *Electrochim. Acta*, 2017, **249**, 253–262, DOI: 10.1016/j.electacta.2017.07.178.

3 X. Wang, C. Liu, C. Gao, K. Yao, S. S. M. Masouleh, R. Berte, H. Ren, L. S. Menezes, E. Cortes, I. C. Bicket, H. Wang, N. Li, Z. Zhang, M. Li, W. Xie, Y. Yu, Y. Fang, S. Zhang, H. Xu, A. Vomiero, Y. Liu, G. A. Botton, S. A. Maier and H. Liang, Self-constructed multiple plasmonic hotspots on an individual fractal to amplify broadband hot electron generation, *ACS Nano*, 2021, **15**, 10553–10564, DOI: 10.1021/acsnano.1c03218.

4 T. Yao, X. An, H. Han, J. Q. Chen and C. Li, Photoelectrocatalytic materials for solar water splitting, *Adv. Energy Mater.*, 2018, **8**, 1800210, DOI: 10.1002/aenm.201800210.

5 H. Sun, Z. Yan, F. Liu, W. Xu, F. Cheng and J. Chen, Self-supported transition-metal-based electrocatalysts for hydrogen and oxygen evolution, *Adv. Mater.*, 2020, **32**, e1806326, DOI: 10.1002/adma.201806326.

6 Y. Zhu, Q. Lin, Y. Zhong, H. A. Tahini, Z. Shao and H. Wang, Metal oxide-based materials as an emerging family of hydrogen evolution electrocatalysts, *Energy Environ. Sci.*, 2020, **13**, 3361–3392, DOI: 10.1039/d0ee02485f.

7 D. Zhou, P. Li, W. Xu, S. Jawaid, J. Mohammed-Ibrahim, W. Liu, Y. Kuang and X. Sun, Recent advances in non-precious metal-based electrodes for alkaline water electrolysis, *ChemNanoMat*, 2020, **6**, 336–355, DOI: 10.1002/cnma.202000010.

8 L. Yang, H. Zhou, X. Qin, X. Guo, G. Cui, A. M. Asiri and X. Sun, Cathodic electrochemical activation of Co_3O_4 nanoarrays: a smart strategy to significantly boost the hydrogen evolution activity, *Chem. Commun.*, 2018, **54**, 2150–2153, DOI: 10.1039/c7cc09416g.

9 C. Liang, P. Zou, A. Nairan, Y. Zhang, J. Liu, K. Liu, S. Hu, F. Kang, H. J. Fan and C. Yang, Exceptional performance of hierarchical Ni–Fe oxyhydroxide@NiFe alloy nanowire array electrocatalysts for large current density water splitting, *Energy Environ. Sci.*, 2020, **13**, 86–95, DOI: 10.1039/c9ee02388g.

10 G. Yanalak, A. Aljabour, E. Aslan, F. Ozel, I. H. Patir, M. Kus and M. Ersoz, NiO and Co_3O_4 nanofiber catalysts for the hydrogen evolution reaction at liquid/liquid interfaces, *Electrochim. Acta*, 2018, **291**, 311–318, DOI: 10.1016/j.electacta.2018.08.130.

11 N. Danilovic, R. Subbaraman, D. Strmcnik, K. C. Chang, A. P. Paulikas, V. R. Stamenkovic and N. M. Markovic, Enhancing the alkaline hydrogen evolution reaction activity through the bifunctionality of $Ni(OH)_2$/metal catalysts, *Angew. Chem., Int. Ed. Engl.*, 2012, **51**, 12495–12498, DOI: 10.1002/anie.201204842.

12 W. Hong, C. Jian, G. Wang, X. He, J. Li, Q. Cai, Z. Wen and W. Liu, Self-supported nanoporous cobalt phosphosulfate electrodes for efficient hydrogen evolution reaction, *Appl. Catal., B*, 2019, **251**, 213–219, DOI: 10.1016/j.apcatb.2019.03.070.

13 Z.-Z. Liu, X. Shang, B. Dong and Y.-M. Chai, Triple Ni-Co-Mo metal sulfides with one-dimensional and hierarchical nanostructures towards highly efficient hydrogen evolution reaction, *J. Catal.*, 2018, **361**, 204–213, DOI: 10.1016/j.jcat.2018.03.004.

14 Y. Wang, B. Zhang, W. Pan, H. Ma and J. Zhang, 3D porous nickel-cobalt nitrides supported on Nickel Foam as efficient electrocatalysts for overall water splitting, *ChemSusChem*, 2017, **10**, 4170–4177, DOI: 10.1002/cssc.201701456.

15 R. Zahra, E. Pervaiz, M. Yang, O. Rabi, Z. Saleem, M. Ali and S. Farrukh, A review on nickel cobalt sulphide and their hybrids: Earth abundant, pH stable electro-catalyst for hydrogen evolution reaction, *Int. J. Hydrogen Energy*, 2020, **45**, 24518–24543, DOI: 10.1016/j.ijhydene.2020.06.236.

16 M. Wang, L. Zhang, Y. He and H. Zhu, Recent advances in transition-metal-sulfide-based bifunctional electrocatalysts for overall water splitting, *J. Mater. Chem. A*, 2021, **9**, 5320–5363, DOI: 10.1039/d0ta12152e.

17 H. Jin, J. Wang, D. Su, Z. Wei, Z. Pang and Y. Wang, In situ cobalt-cobalt oxide/N-doped carbon hybrids as superior bifunctional electrocatalysts for hydrogen and oxygen evolution, *J. Am. Chem. Soc.*, 2015, **137**, 2688–2694, DOI: 10.1021/ja5127165.

18 G. Maduraiveeran, M. Sasidharan and W. Jin, Earth-abundant transition metal and metal oxide nanomaterials: Synthesis and electrochemical applications, *Prog. Mater. Sci.*, 2019, **106**, 100574, DOI: 10.1016/j.pmatsci.2019.100574.

19 J. Hwang, R. R. Rao, L. Giordano, Y. Katayama, Y. Yu and Y. Shao-Horn, Perovskites in catalysis and electrocatalysis, *Science*, 2017, **358**, 751–756, DOI: 10.1126/science.aam7092.

20 M. Han, N. Wang, B. Zhang, Y. Xia, J. Li, J. Han, K. Yao, C. Gao, C. He, Y. Liu, Z. Wang, A. Seifitokaldani, X. Sun and H. Liang, High-valent nickel promoted by atomically embedded copper for efficient water oxidation, *ACS Catal.*, 2020, **10**, 9725–9734, DOI: 10.1021/acscatal.0c01733.

21 J. Li, S. Wang, J. Chang and L. Feng, A review of Ni based powder catalyst for urea oxidation in assisting water splitting reaction, *Adv. Powder. Mater.*, 2022, DOI: 10.1016/j.apmate.2022.01.003.

22 Z. Liu, D. Liu, L. Zhao, J. Tian, J. Yang and L. Feng, Efficient overall water splitting catalyzed by robust $FeNi_3N$ nanoparticles with hollow interiors, *J. Mater. Chem. A*, 2021, **9**, 7750–7758, DOI: 10.1039/d1ta01014j.

23 M. Zha, C. Pei, Q. Wang, G. Hu and L. Feng, Electrochemical oxygen evolution reaction efficiently boosted by selective fluoridation of $FeNi_3$ alloy/oxide hybrid, *J. Energy Chem.*, 2020, **47**, 166–171, DOI: 10.1016/j.jechem.2019.12.008.

24 K. Wang, N. Li, L. Sun, J. Zhang and X. Liu, Free-standing N-doped carbon nanotube films with tunable defects as a high capacity anode for potassium-ion batteries, *ACS Appl. Mater. Interfaces*, 2020, **12**, 37506–37514, DOI: 10.1021/acsami.0c12288.

25 Y. Xu, W. Zheng, X. Liu, L. Zhang, L. Zheng, C. Yang, N. Pinna and J. Zhang, Platinum single atoms on tin oxide ultrathin films for extremely sensitive gas detection, *Mater. Horiz.*, 2020, **7**, 1519–1527, DOI: 10.1039/d0mh00495b.

26 Z. Luo, R. Miao, T. D. Huan, I. M. Mosa, A. S. Poyraz, W. Zhong, J. E. Cloud, D. A. Kriz, S. Thanneeru, J. He, Y. Zhang, R. Ramprasad and S. L. Suib, Mesoporous MoO_{3-x} material as an efficient electrocatalyst for hydrogen evolution reactions, *Adv. Energy Mater.*, 2016, **6**, 1600528, DOI: 10.1002/aenm.201600528.

27 T. Ling, D. Y. Yan, H. Wang, Y. Jiao, Z. Hu, Y. Zheng, L. Zheng, J. Mao, H. Liu, X. W. Du, M. Jaroniec and S. Z. Qiao, Activating cobalt(II) oxide nanorods for efficient electrocatalysis by strain engineering, *Nat. Commun.*, 2017, **8**, 1509, DOI: 10.1038/s41467-017-01872-y.

28 R. Subbaraman, D. Tripkovic, K. C. Chang, D. Strmcnik, A. P. Paulikas, P. Hirunsit, M. Chan, J. Greeley, V. Stamenkovic and N. M. Markovic, Trends in activity for the water electrolyser reactions on 3d M(Ni,Co,Fe,Mn) hydr(oxy)oxide catalysts, *Nat. Mater.*, 2012, **11**, 550–557, DOI: 10.1038/nmat3313.

29 X. Xu, Y. Chen, W. Zhou, Z. Zhu, C. Su, M. Liu and Z. Shao, A perovskite electrocatalyst for efficient hydrogen evolution reaction, *Adv. Mater.*, 2016, **28**, 6442–6448, DOI: 10.1002/adma.201600005.

30 C. Gao, Y. Jiang, C. Sun, J. Han, T. He, Y. Huang, K. Yao, M. Han, X. Wang, Y. Wang, Y. Gao, Y. Liu, M. Yuan and H. Liang, Multifunctional naphthol sulfonic salt incorporated in lead-free 2D tin halide perovskite for red light-emitting diodes, *ACS Photonics*, 2020, **7**, 1915–1922, DOI: 10.1021/acsphotonics.0c00497.

31 C. Xiao, Y. Li, X. Lu and C. Zhao, Bifunctional porous NiFe/$NiCo_2O_4$/Ni Foam electrodes with triple hierarchy and double synergies for efficient whole cell water splitting, *Adv. Funct. Mater.*, 2016, **26**, 3515–3523, DOI: 10.1002/adfm.201505302.

32 X. Zhao, F. Yin, X. He, B. Chen and G. Li, Enhancing hydrogen evolution reaction activity on cobalt oxide in alkaline electrolyte by doping inactive rare-earth metal, *Electrochim. Acta*, 2020, **363**, 137230, DOI: 10.1016/j.electacta.2020.137230.

33 B. H. R. Suryanto, Y. Wang, R. K. Hocking, W. Adamson and C. Zhao, Overall electrochemical splitting of water at the heterogeneous interface of nickel and iron oxide, *Nat. Commun.*, 2019, **10**, 5599, DOI: 10.1038/s41467-019-13415-8.

34 L. Zhang, H. Zhao, S. Xu, Q. Liu, T. Li, Y. Luo, S. Gao, X. Shi, A. M. Asiri and X. Sun, Recent advances in 1D electrospun nanocatalysts for electrochemical water splitting, *Small Struct.*, 2020, **2**, 2000048, DOI: 10.1002/sstr.202000048.

35 Y. Xu, J. Xie, Y. Zhang, F. Tian, C. Yang, W. Zheng, X. Liu, J. Zhang and N. Pinna, Edge-enriched WS_2 nanosheets on carbon nanofibers boosts NO_2 detection at room temperature, *J. Hazard. Mater.*, 2021, **411**, 125120, DOI: 10.1016/j.jhazmat.2021.125120.

36 Z. Wang, M. Li, L. Fan, J. Han and Y. Xiong, Fe/Ni-N-CNFs electrochemical catalyst for oxygen reduction reaction/oxygen evolution reaction in alkaline media, *Appl. Surf. Sci.*, 2017, **401**, 89–99, DOI: 10.1016/j.apsusc.2016.12.242.

37 K. Wang, N. Li, J. Xie, G. Lei, C. Song, S. Wang, P. Dai, X. Liu, J. Zhang and X. Guo, Dual confinement of carbon/TiO_2 hollow shells enables improved lithium storage of Si nanoparticles, *Electrochim. Acta*, 2021, **372**, 137863, DOI: 10.1016/j.electacta.2021.137863.

38 D. Li and Y. Xia, Electrospinning of nanofibers: reinventing the wheel?, *Adv. Mater.*, 2004, **16**, 1151–1170, DOI: 10.1002/adma.200400719.

39 H. Wu, D. Kong, Z. Ruan, P. C. Hsu, S. Wang, Z. Yu, T. J. Carney, L. Hu, S. Fan and Y. Cui, A transparent electrode based on a metal nanotrough network, *Nat. Nanotechnol.*, 2013, **8**, 421–425, DOI: 10.1038/nnano.2013.84.

40 M. A. Z. G. Sial, S. Baskaran, A. Jalil, S. H. Talib, H. Lin, Y. Yao, Q. Zhang, H. Qian, J. Zou and X. Zeng, NiCoFe oxide amorphous nanohetrostructures for oxygen evolution reaction, *Int. J. Hydrogen Energy*, 2019, **44**, 22991–23001, DOI: 10.1016/j.ijhydene.2019.07.018.

41 L. Trotochaud, S. L. Young, J. K. Ranney and S. W. Boettcher, Nickel-iron oxyhydroxide oxygen-evolution electrocatalysts: the role of intentional and incidental iron incorporation, *J. Am. Chem. Soc.*, 2014, **136**, 6744–6753, DOI: 10.1021/ja502379c.

42 X. Cao, T. Wang and L. Jiao, Transition-Metal (Fe, Co, and Ni)-Based Nanofiber Electrocatalysts for Water Splitting, *Adv. Fiber Mater.*, 2021, **3**, 210–228, DOI: 10.1007/s42765-021-00065-z.

43 B. Zhang, Z. Wu, W. Shao, Y. Gao, W. Wang, T. Ma, L. Ma, S. Li, C. Cheng and C. Zhao, Interfacial Atom-Substitution Engineered Transition-Metal Hydroxide Nanofibers with High-Valence Fe for Efficient Electrochemical Water Oxidation, *Angew. Chem., Int. Ed.*, 2021, DOI: 10.1002/anie.202115331.

44 F. Navarro-Pardo, J. B. Liu, O. Abdelkarim, G. S. Selopal, A. Yurtsever, A. C. Tavares, H. G. Zhao, Z. M. M. Wang and F. Rosei, 1D/2D Cobalt-Based Nanohybrids as Electrocatalysts for Hydrogen Generation, *Adv. Funct. Mater.*, 2020, **30**, 1908467, DOI: 10.1002/adfm.201908467.

45 L. L. Wu, Q. S. Wang, J. Li, Y. Long, Y. Liu, S. Y. Song and H. J. Zhang, Co_9S_8 Nanoparticles-Embedded N/S-Codoped Carbon Nanofibers Derived from Metal-Organic Framework-Wrapped CdS Nanowires for Efficient Oxygen Evolution Reaction, *Small*, 2018, **14**, e1704035, DOI: 10.1002/smll.201704035.

46 Y. Tian, A. Huang, Z. Wang, M. Wang, Q. Wu, Y. Shen, Q. Zhu, Y. Fu and M. Wen, Two-dimensional hetero-nanostructured electrocatalyst of Ni/NiFe-layered double oxide for highly efficient hydrogen evolution reaction in alkaline medium, *Chem. Eng. J.*, 2021, **426**, 131827, DOI: 10.1016/j.cej.2021.131827.

47 W. Li, X. Gao, D. Xiong, F. Wei, W.-G. Song, J. Xu and L. Liu, Hydrothermal Synthesis of Monolithic Co_3Se_4 Nanowire Electrodes for Oxygen Evolution and Overall Water Splitting with High Efficiency and Extraordinary Catalytic Stability, *Adv. Energy Mater.*, 2017, **7**, 1602579, DOI: 10.1002/aenm.201602579.

48 J. Huang, J. Han, T. Wu, K. Feng, T. Yao, X. Wang, S. Liu, J. Zhong, Z. Zhang, Y. Zhang and B. Song, Boosting Hydrogen Transfer during Volmer Reaction at Oxides/Metal Nanocomposites for Efficient Alkaline Hydrogen Evolution, *ACS Energy Lett.*, 2019, **4**, 3002–3010, DOI: 10.1021/acsenergylett.9b02359.

49 X. Wang, M. Wang, G. Liu, Y. Zhang, G. Han, A. Vomiero and H. Zhao, Colloidal carbon quantum dots as light absorber for efficient and stable ecofriendly photoelectrochemical hydrogen generation, *Nano Energy*, 2021, **86**, 106122, DOI: 10.1016/j.nanoen.2021.106122.

50 H. Y. Zhao, X. Li, M. K. Cai, C. Liu, Y. M. You, R. Wang, A. I. Channa, F. Lin, D. Huo, G. F. Xu, X. Tong and Z. M. Wang, Role of copper doping in heavy metal-free InP/ZnSe core/shell quantum dots for highly efficient and stable photoelectrochemical cell, *Adv. Energy Mater.*, 2021, **11**, 2101230, DOI: 10.1002/aenm.202101230.

51 X. Li, X. Tong, S. Yue, C. Liu, A. I. Channa, Y. M. You, R. Wang, Z. H. Long, Z. M. Zhang, Z. H. Zhao, X. F. Liu and Z. M. M. Wang, Rational design of colloidal $AgGaS_2$/CdSeS core/shell quantum dots for solar energy conversion and light detection, *Nano Energy*, 2021, **89**, 106392, DOI: 10.1016/j.nanoen.2021.106392.

52 H. Zhao, G. Liu, F. Vidal, Y. Wang and A. Vomiero, Colloidal thick-shell pyramidal quantum dots for efficient hydrogen production, *Nano Energy*, 2018, **53**, 116–124, DOI: 10.1016/j.nanoen.2018.08.042.